The Transition from Shallow to Deep Penetration during Electron Beam Welding

Empirical relationships were developed that can be used to predict penetration depth over a wide range of parameters

BY J. W. ELMER, W. H. GIEDT AND T. W. EAGAR

ABSTRACT. Electron beam partial-penetration welds were made on 2024 aluminum and 304 stainless steel at travel speeds from 6.4 to 3200 mm/s (0.25 to 126 in./s). Different combinations of beam current and travel speed were selected to achieve a wide range of energy densities for three different power density beams, while the use of aluminum and stainless steel provided results for materials with widely different thermal properties. The cross-sectional shapes of the resulting welds were metallographically measured to determine relationships between the welding machine parameters (power, beam diameter and travel speed) and the depth of penetration. The results of this study show that the heating effect of an electron beam can be interpreted as be-

J. W. ELMER is Joining Group Leader, and W. H. GIEDT is a consultant for Lawrence Livermore National Laboratory, Livermore, Calif. T. W. EAGAR is Professor of Materials Engineering, Massachusetts Institute of Technology, Cambridge, Mass.

Paper sponsored by the Department of Energy, IMOG Group, and presented at the 70th Annual AWS Meeting, held April 2-7, 1989, in Washington, D.C.

ing produced by a distributed, point or line heat source, depending on the energy density and the power density of the electron beam. A critical energy density was defined such that, for energy densities below this value, the weld behaves in a distributed-source mode for each of the three power densities studied. However, for energy densities above the critical value, the weld behaves in a point-source mode at low-power densities or in a line-source mode at high-power densities. This critical energy density was found to be a material-dependent property, and it was measured to be 6 J/mm^2 for 2024 Al and 10 J/mm^2 for 304 stainless steel.

KEY WORDS

Electron Beam Welding
Energy Density
Power Density
Critical Energy
Weld Aspect Ratio
Penetration Transition
Shallow Penetration
Deep Penetration
2024 Al EB Welding
304 SS EB Welding

Introduction

Relationships between welding parameters and the geometric shape of the weld pool were investigated by Rosenthal (Ref. 1) in 1946 and Christensen, *et al.* (Ref. 2), in 1965. These studies describe the relationship between the welding machine settings and the geometric shape of the fusion zone for low-power-density arc welds, and the authors utilize the point-source approximation to represent the heating effect of the welding source. This approach assumes an infinite heat-source intensity that is unrealistic; however, despite this assumption, the point-source model predicts the melting-point isotherm reasonably well. Christensen, *et al.*, substantiated this model by experimentally confirming its validity over a wide range of arc welding parameters and material properties.

More realistic physical descriptions of the welding process were later developed to account for the distributed-heat-source nature of the welding arc. For example, Eagar and Tsai (Ref. 3) assumed a Gaussian energy distribution and predicted the geometric shape of welds for distributed heating on the surface of the workpiece. Their model agrees with the point-source solution as the width of the Gaussian dis-

tribution approaches zero, and this complements the point-source solution, allowing the weld-pool shape to be predicted for different welding-power and electrode-gap conditions. This model helped to explain experimental scatter associated with the point-source predictions; however, it is more complicated than the point-source model and requires a numerical integration technique for solution.

Both the point-source and the distributed-source models are based on the assumption that the heating effect is limited to the surface of the workpiece. These conditions exist for low- and intermediate-current arc welds that have power densities of approximately 10^2 W/mm^2. However, this assumption is frequently invalid for high-power-density (HPD) welding conditions that use electron beam (EB) or laser beam (LB) processes. For example, HPD welds can be made at power densities up to 10^5 W/mm^2, and under these conditions the workpiece is vaporized, creating a cavity that allows the heat to be deposited below its surface.

Many investigators have studied the effects that welding parameters have on the depth of penetration in HPD welds. Most of these investigations have been concerned with the deep keyhole mode of penetration, which is generally modeled with the moving-line-source conduction solution for the quasi-steady temperature field. This approach was first applied by Rosenthal (Ref. 1) to model the arc welding of thin plates, and it can also be applied to LB and EB welds when a vapor cavity is formed.

In 1973, Swift-Hook and Gick (Ref. 4) utilized the line-source solution by defining the melt isotherm as a boundary condition that represents the extent of the vapor cavity and surrounding liquid. They applied the resulting equation to LB welds and demonstrated that the model correlates well with experiments, provided the amount of energy absorbed by the workpiece is known. More recently, Giedt and coworkers have studied HPD welds by modeling the vapor cavity and surrounding liquid as a moving elliptical-cylinder (Ref. 5). They accounted for the nonuniform cavity shape with depth of penetra-

tion (Ref. 6), and they experimentally verified their results through a comparison with EB welding data.

Although these studies have been very thorough, there are many examples where the moving line-source and elliptical-cylinder models do not apply. A case in point is EB welds that are made at energy densities that are too low to create a vapor cavity. This situation is common in high-travel-speed welds, and results in penetrations that are more shallow than predicted by the line-source models. Under these conditions, the heat is transferred primarily to the surface of the workpiece, and the resulting welds may have depth-to-width ratios less than 1:10 (Ref. 7). For both the deep and shallow penetration cases, the depth-to-width ratio varies considerably from its ideal value of 1:2 predicted by the point-source solutions.

This study was initiated to investigate the parameters that control the geometric shape of the fusion zone in EB welds over the wide range of conditions that are available with current welding equipment. The objectives of the study were: 1) to define the conditions for the transition of heat-distribution modes during EB welding, based on the average energy density and the average power density incident on the surface of the workpiece; and 2) to determine relationships between the welding parameters and penetration for both the high-energy-density keyhole and the low-energy-density surface-modification conditions. The results of this study emphasize the wide range of cross-sectional fusion zone shapes that can be produced by the EB process and show that these shapes can be predicted from the EB welding parameters.

Experimental Procedure

High-Power-Density Welding Parameters

Three parameters were used to characterize the HPD process: 1) the power density incident on the workpiece, P_0, 2) the energy density absorbed by the workpiece, E_0, and 3) the energy absorbed per unit length of weld, E_L. In this investigation, the average value of the energy density, power density and energy per unit length of weld will be used to represent the heating effect of the electron beam, and these parameters will be denoted by a bar placed over the appropriate symbol.

The average power density, $\bar{P}_0$, is the ratio of the EB power, P, to the beam area, A, at the workpiece surface:

$$\bar{P}_0 = P/A, \tag{1}$$

where P is defined as the product of the accelerating voltage and the EB current (P = I × V), and where A is the area of a circle of focal spot diameter f.

The average energy density, $\bar{E}_0$, is the average amount of energy absorbed per

unit area on the surface of the workpiece:

$$\bar{E}_0 = P/fS, \tag{2}$$

where S is the travel speed of the workpiece and f is again the focal spot diameter. This equation assumes that the efficiency of the electron beam (ratio of the energy incident on the surface of the metal to the energy absorbed by the metal) is unity. Actual EB efficiencies are typically about 0.95 for stainless steel alloys (Ref. 4).

Finally, the average energy absorbed per unit length of weld, $\bar{E}_L$, is the product of the average energy density and the focal spot diameter:

$$\bar{E}_L = P/S. \tag{3}$$

For the purpose of calculating effects of EB parameters on the shape of the fusion zone, $\bar{E}_0$, $\bar{P}_0$, and $\bar{E}_L$ are important because they influence heat distribution mode.

Beam Diameter and Power Density

The effective beam diameter was measured by sharply focusing the beam on a tungsten block and measuring the diameter through the 5× magnifying optics. These observations show that the highest-intensity light is emitted from a disk-shaped region at the center of the beam. Outside this region, the intensity of the emitted light decreases quickly in a narrow "halo" that surrounds the center of the electron beam. The center disk of the electron beam was used as the parameter to represent the beam diameter, and the disk was measured at 100 kV for six EB currents ranging from 3 to 14 mA.

Measurements of EB current-density distributions, made with a modified Faraday cup, suggest that the tungsten block is only accurate for EB diameters for beam currents below about 10 mA (Ref. 8). At higher current levels, the true beam diameter is less than that measured on the tungsten block; therefore, corrections were required for the diameters measured on the high current beams.

The measured and corrected focal spot diameters are listed in Table 1, showing that the 12 and 14 mA beam diameters were reduced 12% and 18%, respectively. These corrected values are consistent with the extrapolated values of the lower mA beam diameters, and they are qualitatively consistent with the modified Faraday cup results of Burgardt (Ref. 8). The average power density was calculated from the corrected focal spot diameters using Equation 1, and the results show that $\bar{P}_0$ increases with increasing EB current from about 4.0×10^3 W/mm^2 at 3 mA to 5.7×10^3 W/mm^2 at 14 mA.

Material Properties

The EB tests were bead-on-plate welds made on Type 304 stainless steel (68.8 Fe,

Table 1—Beam Diameter and Average Power Density as a Function of Beam Current at 100 kV

Beam Current (mA)	f Measured (mm)	f Corrected (mm)	$\bar{P}_0$ (W/mm^2)
14	0.68	0.56	5680
12	0.60	0.53	5440
7	0.43	0.43	4840
6	0.40	0.40	4760
3.5	0.33	0.33	4080
3	0.31	0.31	3980

10.2 Ni, 18.0 Cr, 1.7 Mn, 0.051 C, and 0.055 N wt-%) and Type 2024 aluminum (92.5 Al, 4.30 Cu, 1.65 Mg, 0.27 Fe, 0.18 Si, 0.02 Cr wt-%). The chemical compositions of the specimens used were measured by emission spectroscopy and gasfusion interstitial analysis. Physical property data for these alloys are listed in Table 2, representing the average value between room temperature and the melting temperature (Refs. 6, 9). In Table 2, k is the thermal conductivity, H_f is the latent heat of fusion, C_p is the heat capacity, ρ is the density, α is the thermal diffusivity, and Θ_M is the temperature rise in the workpiece.

EB Machine Settings

Single-pass welds were made across the 38-mm (1.5-in.) width of 6.3-mm (0.25-in.) thick coupons, using an electron beam that was focused on the surface of the coupon. The EB test conditions are summarized in Table 3, which gives the travel speed, the beam current and the average energy per unit length of weld for 30 different test conditions on each alloy. These tests were conducted at three different power levels and ten travel speeds to produce a wide range of energy densities. These tests were conducted on a Hamilton-Standard model W-2 welding machine, with a hairpin filament.

Results

The locations on the weld pool that define the melt depth (D), width (W) and length (L) are illustrated in Fig. 1. Each of these dimensions was measured on the resolidified melts by postweld metallographic analysis, and the results are summarized in Table 4.

The depth and width of the weld pools were measured from metallographic cross-sections taken on the plane perpendicular to the welding direction. The lengths of the low-speed weld pools (S < 100 mm/s) were metallographically measured on longitudinal sections along the center of the fusion zone.

The length of the high-speed weld pools (S > 100 mm/s) could not be metallographically measured because of a lack of solidification striations at high speeds. Therefore, the lengths of these weld pools were estimated from the weld ripple lags on the surfaces of the workpieces at 50X magnification.

Interpretation of Results

Operating Parameter Relationships

The geometric shapes of the EB weld pools were compared with distributed source, point source, and line source heat-conduction models. These comparisons indicate that each model can be used to represent certain EB welding regimes, but that none of the models can be used

to represent all of the data. These models represent the three basic heating-source modes, and will be used as references to compare the experimental data.

Prior to introduction of these models, the EB data will first be plotted on one set of coordinates to illustrate the inability of a single model to represent the geometric shape of EB welds that are made over a wide range of travel speeds. Here, the coordinates that were selected to represent the data are those developed by Christensen, et al. (Ref. 2), and they are referred to as operating parameter plots.

The thermal properties of the material influence the rate at which heat is transferred from the surface, and therefore they influence the geometric shape of the weld pool. Christensen, et al., accounted for the thermal properties of different alloys by defining dimensionless parameters that are analogous to the thermal Peclet number for forced convection in fluid dynamics. These were a dimensionless depth (D*), width (W*) and length (L*), which are related to the actual depth (D), width (W) and length (L) of the weld pool as follows:

$$D^* = \frac{SD}{2\alpha}; \ W^* = \frac{SW}{2\alpha}; \ L^* = \frac{SL}{2\alpha}, \quad (4a,b,c)$$

where S is the travel speed and α is the

thermal diffusivity of the solid.

The power of the heat source was included in a dimensionless "operating parameter," n, which was defined as follows:

$$n = \frac{PS}{4\pi\alpha^2 C_p\Theta_M\rho}, \quad (5)$$

where the quantity $C_p\Theta_M\rho$ is the amount of heat required to bring the alloy up to the melting temperature, and it is sometimes modified by adding to it the latent heat of fusion. This operating parameter is related to the heat source strength, but it does not account for the distribution of energy to the workpiece.

The dimensionless quantities represented by Equations 4 and 5 were used to

Property	Units	Stainless Steel	Al
ρ	(g/mm^3)	0.0079	0.0027
k	W/mm K	0.025	0.175
H_F	(J/mm^3)	2.13	1.07
C_p	(J/g K)	0.5	1.05
$\alpha = k/(\rho C_P)$	(mm^2/s)	4.5	67
$\Theta_M = T_M - T_0$	(K)	1408	570
$H_M = \rho C_p\Theta_M + H_F$	(J/mm^3)	7.70	2.68

Table 3—Electron Beam Test Conditions

Weld	Stainless Steel			Al		
	Speed (mm/s)	Current (mA)	$\bar{E}_L$ (J/mm)	Speed (mm/s)	Current (mA)	$\bar{E}_L$ (J/mm)
1		3.5	55		3.0	47
2	6.4	7.0	110	6.4	6.0	94
3		14.0	220		12.0	189
4		3.5	28		3.0	24
5	12.7	7.0	55	12.7	6.0	47
6		14.0	110		12.0	94
7		3.5	14		3.0	12
8	25.4	7.0	28	25.4	6.0	24
9		14.0	55		12.0	47
10		3.5	6.9		3.0	6
11	50.8	7.0	14	50.8	6.0	12
12		14.0	28		12.0	24
13		3.5	3.5		3.0	3.0
14	100	7.0	7.0	100	6.0	6.0
15		14.0	14		12.0	12
16		3.5	1.75		3.0	1.5
17	200	7.0	3.5	200	6.0	3.0
18		14.0	7.0		12.0	6.0
19		3.5	0.88		3.0	0.75
20	400	7.0	1.75	400	6.0	1.5
21		14.0	3.5		12.0	3.0
22		3.5	0.44		3.0	0.38
23	800	7.0	0.88	800	6.0	0.75
24		14	1.75		12.0	1.5
25		3.5	0.22		3.0	0.19
26	1600	7.0	0.44	1600	6.0	0.38
27		14.0	0.88		12.0	0.75
28		3.5	0.055		3.0	0.047
29	3200	7.0	0.11	3200	6.0	0.094
30		14.0	0.22		12.0	0.19

Table 4—Weld Pool Dimensions (mm)

| Weld	Stainless Steel Depth (mm)	Width (mm)	Length (mm)	Al Depth (mm)	Width (mm)	Length (mm)
1	1.16	2.10	2.30	0.85	1.66	1.2
2	4.22	2.40	2.80	4.05	2.20	2.10
3	8.10	2.70	6.00	12.0	3.20	3.90
4	0.51	1.36	1.80	0.75	1.40	1.10
5	1.30	1.70	3.20	3.40	1.92	1.91
6	5.20	2.28	4.60	10.5	3.16	3.50
7	0.61	1.08	1.50	0.61	1.24	0.81
8	1.68	1.46	3.10	3.10	1.88	2.22
9	3.60	1.80	5.30	8.10	2.54	3.74
10	0.46	0.96	1.60	0.49	1.00	0.76
11	0.95	1.16	3.40	1.86	1.50	1.93
12	2.05	1.46	4.50	4.95	2.20	2.80
13	0.39	0.67	1.71	0.39	0.84	0.78
14	0.73	0.93	3.10	1.08	1.44	1.88
15	1.29	1.26	3.90	3.10	2.10	3.90
16	0.24	0.50	1.16	0.35	0.76	0:45
17	0.44	0.84	2.81	0.99	1.38	1.70
18	0.67	1.22	x	1.40	1.85	4.23
19	0.15	0.38	1.10	0.30	0.70	0.48
20	0.23	0.77	2.73	0.70	1.30	1.70
21	0.30	1.05	x	0.88	1.65	4.50
22	0.060	0.27	0.86	0.25	0.66	0.40
23	0.088	0.70	1.63	0.36	1.20	1.55
24	0.15	1.05	x	0.55	1.42	5.25
25	0.040	0.14	0.2	0.10	0.30	0.25
26	0.060	0.46	0.39	0.15	0.70	0.78
27	0.095	0.95	x	0.23	1.20	2.97
28	x	x	x	x	x	x
29	x	x	x	x	x	x
30	0.040	0.90	x	0.10	0.91	2.35

compare the characteristics of the EB welds by plotting the dimensionless variables vs. the operating parameter on Log-Log coordinates.

The dimensionless depth vs. the operating parameter is plotted in Fig. 2A for the Al alloy welds. These data show that the EB power level influences D* under constant operating parameter conditions. Here, the lowest-power welds correspond reasonably well with the Christensen, et al., results. However, as the power level is increased, the weld penetration deviates to higher dimensionless depths under constant operating-parameter conditions. Furthermore, at high travel speeds (high n), the dimensionless depth decreases to zero.

The dimensionless width vs. the operating parameter is shown in Fig. 2B for the Al alloy welds. It is obvious that the EB power level also has an effect on W*. However, for constant operating parameter conditions, the dimensionless width decreases with increasing power level of the electron beam. This behavior is opposite to that of the depth and is related to the keyholing effect in the HPD welds.
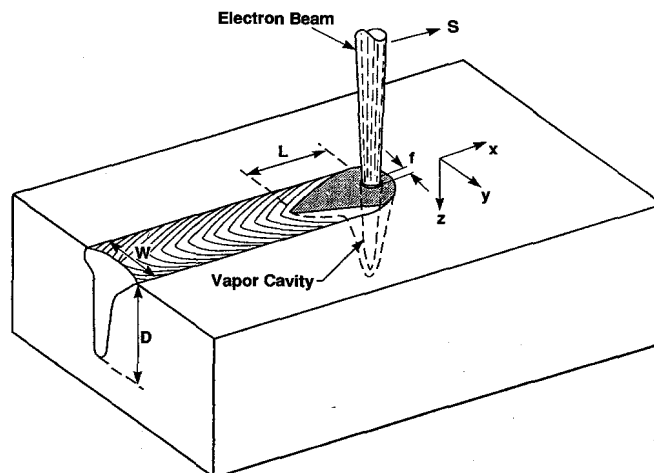
These graphs clearly demonstrate that the dimensionless depth and width depend on the power level of the electron beam for a given operating parameter. This inability of n to uniquely define the fusion zone shape is related to the fact that n is not a direct measure of the energy deposited in the workpiece. This is because the operating parameter incorporates both the travel speed and the power in its numerator: thus, n increases with increasing travel speed and n increases with increasing power. Therefore, with increasing travel speed S and fixed power P, n would increase, but the dimensionless depth would decrease to zero. Indeed, the trend would be different if the increase in n were due to an increase in P at constant S.

A more descriptive measure of the relationship between the welding parameters and the depth of penetration incorporates the energy density and power density of the electron beam. Since neither of these parameters is included in the definition of the dimensionless quantities, a different interpretation of HPD weld behavior is required.

Energy Density Relationships

The average energy density in the electron beam, $\bar{E}_0 = (P/fS)$, was found to be important in identifying relationships between the welding power and travel speed and weld pool shape. The weld depth and width all increase with $\bar{E}_0$, and the following results will show that the average energy density in the electron beam is sufficient to characterize the weld pool depth for low-energy-density welds. However, for high-energy-density welds, $\bar{E}_0$ alone is not sufficient to characterize the weld pool depth. Under these conditions, both the average energy density and the average power density must be considered in describing the fusion zone shape.

The depth and half-width of the EB welds are plotted vs. $\bar{E}_0$ on Log-Log coordinates in Figs. 3 and 4. Each of these graphs includes three sets of symbols and the best-fit lines through each set of symbols. Each best-fit line identifies the results for a constant EB power level,[1] for which the energy density has been varied by changing the travel speed of the electron beam. At high speeds, the energy density is low and the depth of penetration is low. At low speeds, the energy density is high and the depth of penetration is high.

The influence of energy density on the depth of penetration of the stainless steel alloy is shown in Fig. 3A. This plot exhibits three energy-density regimes: 1) at energy

Fig. 1—Schematic representation of an electron beam weld. The length (L), depth (D) and width (W) of the weld are indicated for the electron beam moving in the positive X-direction at travel speed S.

Electron Beam

S

L

f

x

y

z

W

Vapor Cavity

D

---

[1]Note that a given EB power level corresponds to a specific power density, as summarized in Table 1.
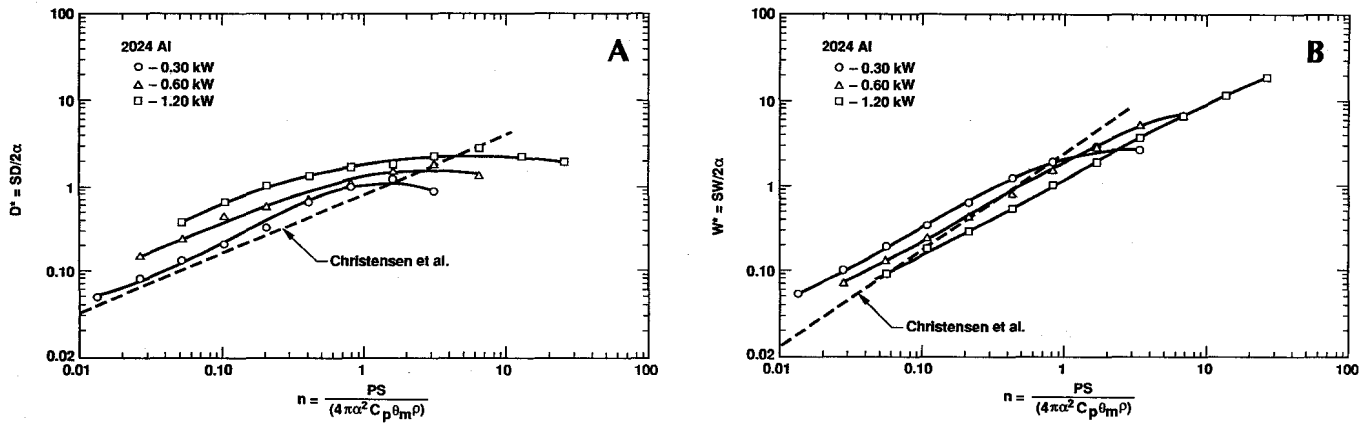
Fig. 2 — A — Dimensionless depth and B — dimensionless width of the 2024 Al welds, plotted vs. the operating parameter. Three EB power levels are indicated and the results are compared with the results of Christensen, et al. (dashed lines).

densities below 1 J/mm², no melting is observed; the workpiece is rapidly heated to a temperature below its melting point and rapidly cools to ambient conditions, 2) between 1 J/mm² and 10 J/mm², the alloy melts and the depth of penetration increases with increasing energy density. In this regime, the energy density alone is sufficient to characterize the melt pool depth, and the penetration is nearly independent of the power density of the electron beam and 3) above 10 J/mm², the depth continues to increase with energy density, but the rate at which the depth increases with energy density de-

pends on the power density of the electron beam. In this regime, higher power densities result in deeper welds, under constant energy-density conditions.

The influence of energy density on the fusion-zone half-width of the stainless steel alloy is shown in Fig. 3B. The width of the EB welds also shows different regions of behavior. At low energy densities, the width depends on both the energy density and the power density of the beam. In this regime, the width of the molten zone increases with increasing power density under constant energy-density conditions. As the energy density increases, the weld

width becomes less dependent on the power level under constant energy-density conditions.

The depth and half-width of welds in 2024 Al are plotted vs. the energy density in Figs. 4A and 4B, respectively. The results for the aluminum alloy are similar to those of the stainless steel alloy. An average energy density of approximately 1 J/mm² is required to initiate melting. As the energy density increases above this value, the increase in penetration is initially dependent only on the energy density. However, as the energy density increases, the penetration depends on both the energy
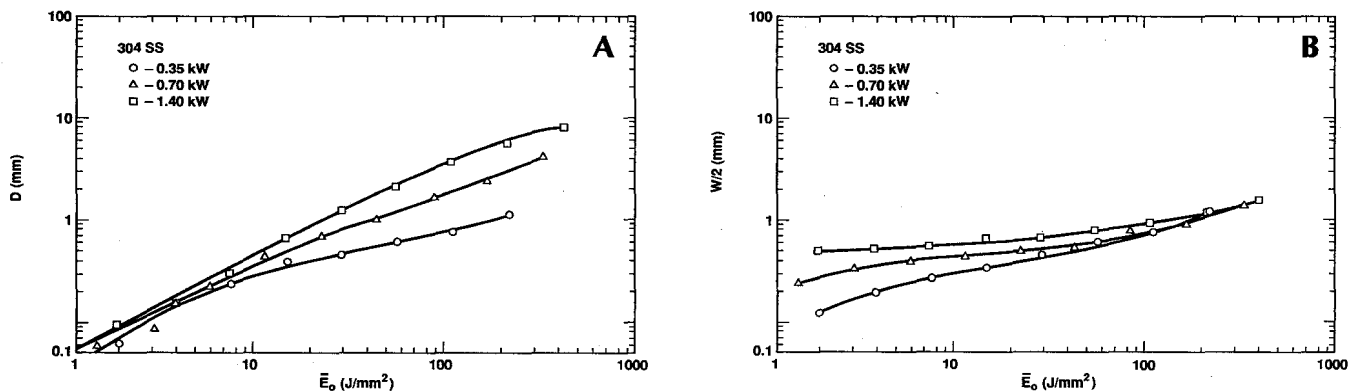

Fig. 3 — A — Weld depth and B — weld half-width plotted vs. the average energy density for the 304 stainless steel alloy.
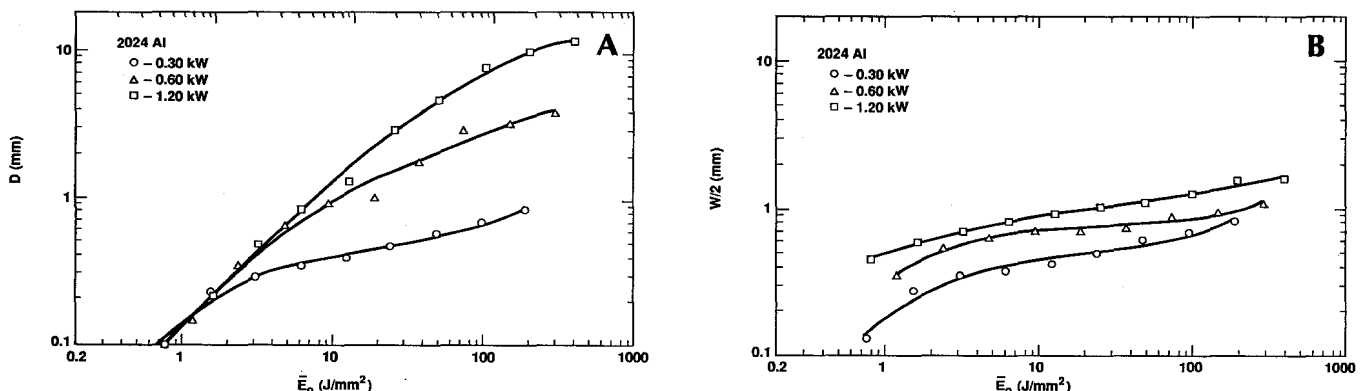

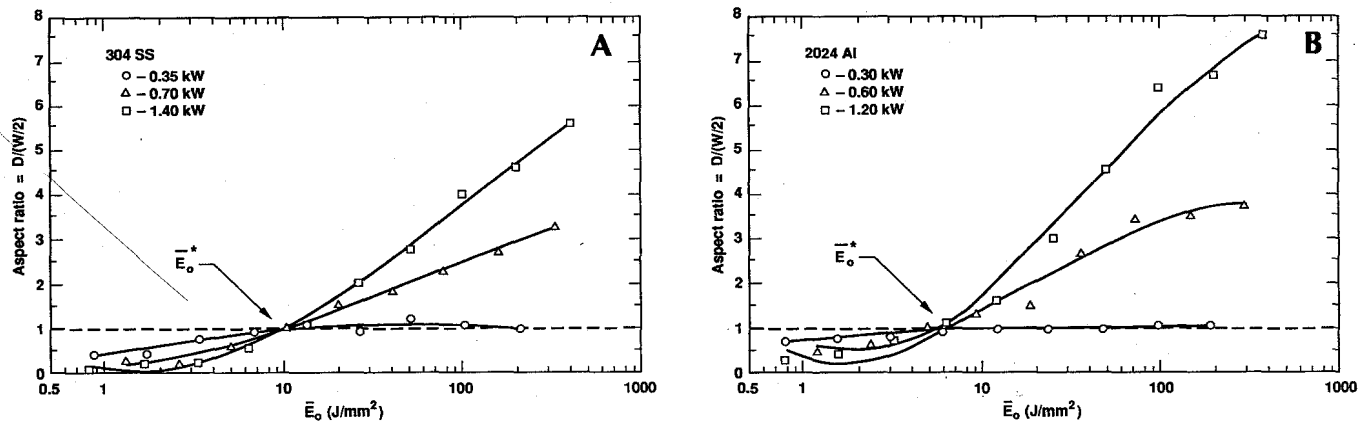Fig. 4 — A — Weld depth and b — weld half-width plotted vs. the average energy density for the 2024 Al alloy.

Fig. 5 — Weld aspect ratio plotted vs. the average energy density for A — 304 stainless steel and B — 2024 Al. The critical energy density, $\bar{E}^*_0$, is indicated, and the dashed lines give the aspect ratio for ideal point-source welds.

density and the power density of the electron beam.

The Critical Energy Density for Distributed-Source to Line-Source Transition

The results of the preceding section can be generalized by plotting the aspect ratio of the welds vs. the average energy density. For convenience, the aspect ratio, ϕ, will be defined as the depth of penetration to the half-width of the EB weld:

$$\phi = D/(W/2). \qquad (6)$$

The half-width, rather than the full width, is used so that $\phi = 1.0$ for an ideal point-source weld can be used as a reference for comparison with other welds. For aspect ratios less than unity, energy is being distributed on the surface of the workpiece, whereas for aspect ratios greater than unity, energy is being deposited below the surface of the workpiece.

The aspect ratio of the 304 stainless steel alloy welds is plotted vs. the average energy density in Fig. 5A. These results are compared to a horizontal-dashed line, which represents the ideal aspect ratio of 1.0 predicted by the point-source model. It is clear that a transition in the heat-distribution mode occurs at $\bar{E}^*_0 = 10$ J/mm^2. For $\bar{E}_0 < \bar{E}^*_0$, the aspect ratio is less than that predicted by the point-source model; for $\bar{E}_0 > \bar{E}^*_0$, the aspect ratio is greater than that predicted by the point-source model. One exception to this behavior occurs for the lowest-power-density welds, which maintain an aspect ratio of about unity, up to energy densities as high as 200 J/mm^2.

The aspect ratio of the 2024 Al alloy welds is plotted vs. the average energy density in Fig. 5B. These results are similar to the 304 stainless steel alloy with $\bar{E}^*_0 = 6$ J/mm^2. Overall, the aluminum alloy begins to keyhole at lower energy densities and has higher aspect ratios than the stainless steel alloy. The lowest-power-density weld also maintains an aspect ratio close to unity for $\bar{E}_0 > \bar{E}^*_0$.

It is clear that a transition in the weld behavior occurs at $\bar{E}_0$ of about 10 J/mm^2 in the stainless steel alloy and about 6 J/mm^2 in the Al alloy. This transition value will be defined as the critical energy density, $\bar{E}^*_0$, and it represents the ED for the transition from distributed to line heat-distribution modes. For $\bar{E}_0 < \bar{E}^*_0$, the EB welds have characteristics of a distributed heat source with aspect ratios less than unity. In this regime, lower energy densities result in lower-aspect-ratio welds. For $\bar{E}_0 > \bar{E}^*_0$, the welds are characteristic of line-source heating, and the depth of the line increases with increasing energy density. The power density also plays a role with respect to the heat input mode. Above $\bar{E}^*_0$, the aspect ratio increases with $\bar{E}_0$ and with $\bar{P}_0$ such that, at low values of $\bar{P}_0$, the heat-input mode can be simulated as a point source, with weld aspect ratios equal to 1.0; however, at high power levels, the heat input must be simulated by a line source, with weld aspect ratios greater than 1.0.

Discussion

Penetration Based on Point-Source and Line-Source Theory

The relationships between the depth of penetration and the energy input for ideal point-source heating and ideal line-source heating will first be presented. These predictions will then be used as references for interpretation of the experimental results.

The depth of penetration for point-source welds can be determined from the solution for the temperature distribution surrounding a point heat source in a semi-infinite plate that is moving at speed S in the X direction (Ref. 1):

$$T - T_0 = \frac{P}{2\pi k R} e^{\left(\frac{-S(R + X)}{2\alpha}\right)}, \qquad (7)$$

where $T - T_0$ is the temperature rise in the workpiece, R is the radial distance from the heat source, and X is the distance behind the heat source. Substituting the

liquidus temperature, T_M, for T, yields a specific relation for the melt isotherm; points on the melted isotherm are denoted by a subscript M.

A second subscript, B, will be used to further indicate the points of the melt isotherm that lie on the melt boundary (sometimes referred to as the melt periphery). This melt boundary is the locus of points that define the maximum girth of the melt isotherm, and this feature is the weld pool 'shape' that is observed in a metallographic cross-section.

The maximum penetration lies on the melt boundary, and can be determined from the following equations (which are reviewed in the appendix):

$$D = (R^2_{MB} - X^2_{MB})^{1/2}, \qquad (8)$$

where R_{MB} is the radial distance from the point source to the melt boundary and is defined by the following relationship:

$$R_{MB} = \left(\frac{P}{2\pi k \theta_M}\right) e^{\left(\frac{-SR_{MB}}{SR_{MB} + 2\alpha}\right)}, \qquad (9)$$

and where X_{MB} is the distance of the melt boundary behind the heat source:

$$X_{MB} = \frac{-SR^2_{MB}}{SR_{MB} + 2\alpha}. \qquad (10)$$

Note that R_{MB} can be calculated from Equation 9 using an iterative approach, given set of material properties (α, k, θ_M) and processing parameters (P, S).

Using these equations, the maximum depth of penetration can be calculated from the welding parameters and the thermal properties of the workpiece. Furthermore, the variation in D, for a wide range of processing parameters and material properties, can be conveniently shown using the following dimensionless groups (Ref. 6):

$$\frac{P}{Dk\theta_M} \text{ and } \frac{SW}{\alpha}. \qquad (11a, 11b)$$

The first parameter, which includes the power-to-depth ratio, will be plotted on the Y-axis. The second parameter is di-

rectly proportional to the weld width and travel speed, and will be plotted on the X-axis.

The variation of $P/(Dk\theta_M)$ with (SW/α), as determined by Equations (8-10) for a point source, is shown as the dashed line in Fig. 6. Two regimes and a transition between these regimes are apparent from this curve. At low values of the X-axis dimensionless group (low travel speeds), the point-source relationship asymptotically approaches a slope of zero at a Y-axis value of 2π. At high values of the X-axis dimensionless group (high travel speeds), the curve approaches a slope of unity.

The variation of $P/(Dk\theta_M)$ with (SW/α) for the line-source equation was derived for a conical-shaped fusion zone by Giedt and Tallerico (Ref. 6), and is plotted as the solid line in Fig. 6. For high X-axis values, the line-source curve also approaches a slope of unity; and for low X-axis values, the curve approaches a slope of zero. This behavior is similar to that of the point-source theory, with the exception that line-source heating results in lower Y-axis values for a given X-axis parameter. Since the Y-axis is inversely proportional to the depth of penetration, the line-source theory predicts deeper penetrations for welds operating in the line-source mode than for those in the point-source mode.

Predicting the Penetration of EB Welds

Relationships between the dimensionless groups of Equations 11a and 11b can be used to predict weld depth only if the weld width is known. Since the weld width is not known *a priori*, an approximation of the weld width must be made in order to predict the weld depth. As an alternative approach, it is proposed to substitute the focal spot diameter, f, for the weld fusion zone width; W: *i.e.*, to specify the independent X-axis coordinate as:
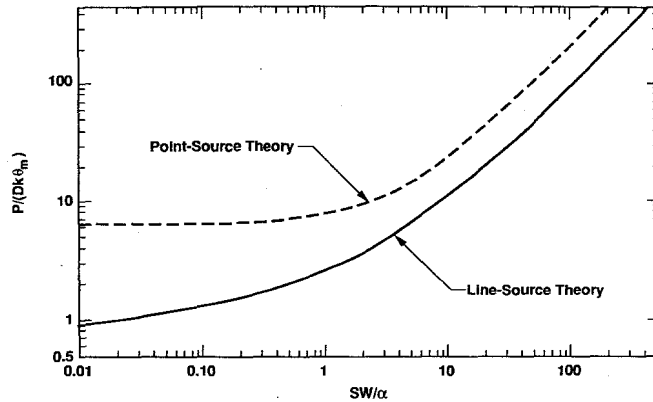
$$\frac{Sf}{\alpha} \qquad (12)$$

This definition was used because: 1) f can be easily measured prior to making the weld and 2) f is related to the energy density incident on the surface of the base metal substrate.

All of the EB data are plotted in Figs. 7A and 7B using $X = (Sf/\alpha)$. In these graphs, large values of the X-axis dimensionless group correspond to the welds made at high travel speeds, and these have low energy densities with shallow penetrations. Small values of the X-axis dimensionless group correspond to low travel speeds, and these have high energy densities with deep penetrations.

Uniform Distributed Source Regime

The first welds to be analyzed are those made at high travel speeds $((Sf/\alpha) > 20$ for the stainless steel alloy and $(Sf/\alpha) > 3$ for the Al alloy). These data are fitted by a solid line having a slope equal to 1.0 in Fig. 7, indicating that the penetration is directly proportional to P/Sf. Therefore, the penetration can be described by the following relationship:

$$D = \left(\frac{1}{C}\right)\left(\frac{\alpha}{k\theta_M}\right)\left(\frac{P}{(Sf)}\right). \qquad (13)$$

The constant C is different for the two alloys: it was determined to be 2.0 for the

stainless steel alloy and 3.6 for the Al alloy, where D is in mm, the material-property units are summarized in Table 2, and the EB parameters are in units of mm, J and s.

The combination of process parameters, P/Sf, was previously defined as the average energy density of the electron beam $\bar{E}_0$. By substituting this relationship and the relationship $(\alpha/(k\theta_M)) = (1/\rho C_p\theta_M)$, the experimentally determined penetration of the EB welds can be represented by the following equation:

$$D = \left(\frac{1}{C}\right)\left(\frac{1}{\rho C_p\theta_M}\right)(\bar{E}_0). \qquad (14)$$

This equation is simply a different form of Equation 13, and indicates that the penetration is proportional to the ratio of $\bar{E}_0$ to the amount of heat required to bring the alloy to its solidus temperature. This result is easily derived from a one-dimensional energy balance normal to the surface of the workpiece by assuming that the heat is distributed uniformly on the surface of the workpiece and that the penetration depth is small compared to the focal spot diameter.

The Al and stainless steel data were further analyzed by including the latent heat of fusion, H_f, in Equation 14. This factor was incorporated by defining a new parameter, H_M, which represents the amount
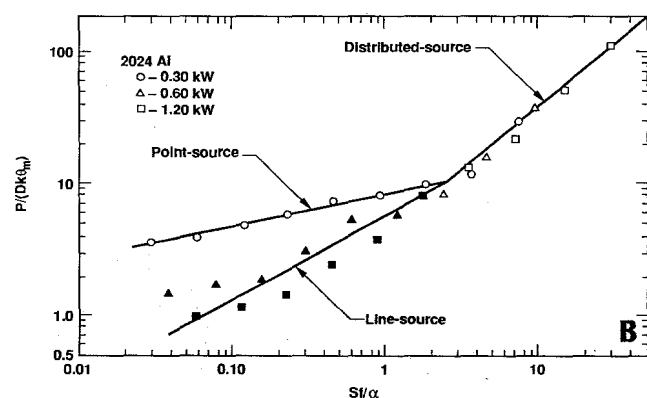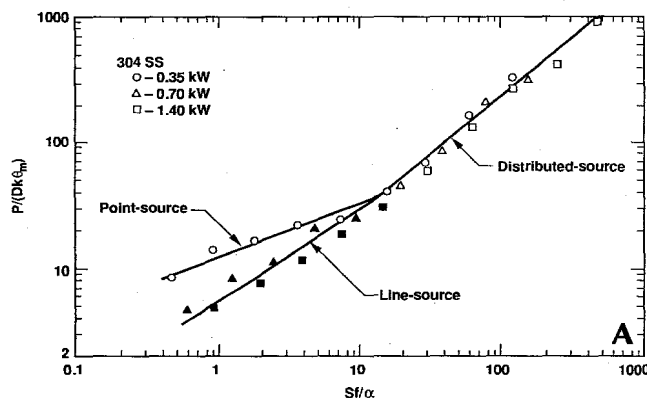
Fig. 7 — Electron beam weld results plotted on dimensionless coordinates that incorporate: 1) the power-to-depth ratio on the Y-axis and 2) the product of the focal spot diameter and travel speed on the X-axis. A — shows the results of the 304 stainless steel welds; B — shows the results of the 2024 Al welds. The solid symbols refer to the line-source welds ($\phi > 1$); the open symbols refer to the distributed- and point-source welds ($\phi < 1$).

Fig. 8 — Depth of penetration for distributed-source welds plotted vs. the ratio of the average energy density to the heat required to melt the alloy.
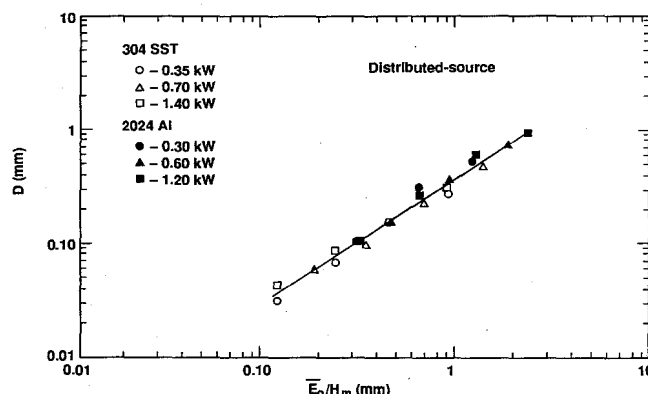
of energy required to heat the alloy to its melting temperature and to subsequently melt the alloy:

$$H_M = (\rho C_p \theta_M + H_f) \qquad (15)$$

Plotting the actual low-energy-density weld data vs. $\bar{E}_0/H_M$ allowed the penetration for both the stainless steel and the Al alloys to be predicted by one equation. These results are shown in Fig. 8, which indicates that $C = 2.43$ and that the data have a slope of approximately unity on these coordinates. The proportionality constant $C = 2.43$ represents the average behavior of both the stainless steel and the Al alloys, and the depth of penetration takes the following form:

$$D = \left(\frac{1}{2.43}\right)\left(\frac{1}{H_M}\right)(\bar{E}_0), \qquad (16)$$

where D is in mm, the appropriate material property units are summarized in Table 2, and $\bar{E}_0$ is in J/mm².

Point-Source Regime

The low power welds made at energy densities above $\bar{E}^*_0$, follow the trends established for a point source because they have aspect ratios close to unity — Fig. 5. As indicated in Fig. 7, these welds penetrate less than welds of either the line source or the distributed source type under similar welding conditions. Furthermore, the variation of Log $P/(Dk\theta_M)$ with

Log Sf/α has a much more shallow slope for the point-source welding conditions.

Figure 9 plots the depth of the actual welds that had aspect ratios close to unity vs. $\bar{E}_0/H_M$ on Log-Log coordinates. Unlike the distributed-source welds, these results indicate that the stainless steel alloy and the Al alloy cannot be described by a single equation on these coordinates.

Fitting the data presented in Fig. 9 by regression analysis yields the following relation:

$$D = \left(\frac{1}{C}\right)\left(\frac{\bar{E}_0}{H_M}\right)^m \qquad (17)$$

where the constant C was determined to be 3.2 for the stainless steel alloy and 3.5 for the Al alloy, and the slope m was determined to be 0.36 for the stainless steel alloy and 0.28 for the Al alloy. In this equation, D is given in mm, $\bar{E}_0$ is in J/mm², and the appropriate material-property units are summarized in Table 2.

The different relationships for the two alloys result from the fact that the widely different thermal properties between the Al and stainless steel alloys place them in different locations in the point-source transition region. Figure 6 showed the relationship between Log $P/(Dk\theta_M)$ with Log Sf/α for ideal point-source heating. At high values of the travel speed, the slope of this graph approaches 1, while at low travel speeds, the slope approaches 0. The transition region between the limiting
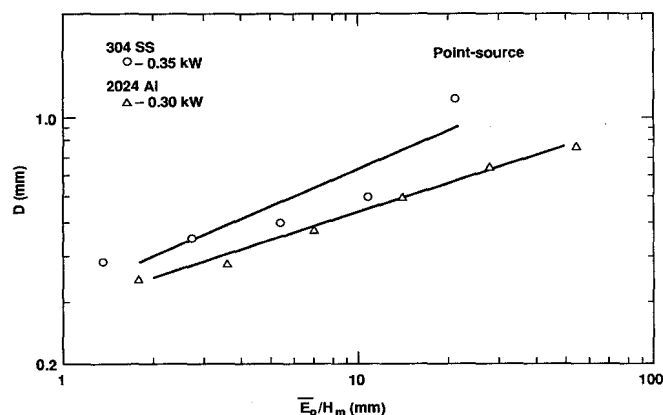
slopes occurs for X-axis dimensionless group (SW/α) values between 0.2 and 20. In this region, there is a nonlinearity on the Log-Log coordinates between the depth of penetration and the travel speed for constant-power welds. This nonlinearity makes it difficult to predict the penetration behavior of materials with different thermal properties that have different (SW/α) values in this regime.

The actual point-source-weld data falls largely within this transition region; therefore, one would expect the trend in the weld pool shape to depend on the specific value of the X-axis dimensionless group for these welds. Also, because of the large difference in thermal diffusivities between the SST and the Al alloys, the X-axis values for these two alloys are separated by about a factor of 15 for identical welding conditions. Thus, the relationship between penetration and travel speed for a given power level is different for these two alloys, and leads to the different coefficients for Equation 17. Furthermore, extrapolation of the penetration predictions beyond the measured values represented by Equation 17 would not necessarily lead to good estimations of the weld depth.

Line-Source Regime

The moving-line heat-source equation used by Giedt and Tallerico (Ref. 6) assumes a conical-shaped fusion zone of width W at the surface of the workpiece. The mathematical description of this model yields the same two dimensionless groups that were used to represent the point-source welds in Equations 11a and 11b.

Using these equations, Giedt and Tallerico compared the results of actual keyhole penetration welds in several different alloys (Ref. 6), and they developed the following empirical relationship from their observations:

$$\frac{P}{Dk\theta_M} = (3.3)\left(\frac{SW}{\alpha}\right)^{0.625} \qquad (18)$$

This relationship has a slope of 0.625 when the dimensionless groups are plotted on Log-Log coordinates, and it correlates well with their line-source-theory model over the range of parameters investigated.

In Figures 7A and 7B, the solid symbols represent the welds that behaved in a keyhole mode with aspect ratios greater than 1.0. The slope of 0.625 on these coordinates (determined by Giedt and Tallerico) is drawn through the solid symbols for comparison. This slope also fits the experimental keyhole welds of this investigation, and this slope was used to derive a relationship between penetration and the EB parameters for keyhole welds pro-

Fig. 9 — Depth of penetration for the point-source welds plotted vs. the ratio of the average energy density to the heat required to melt the alloy.

duced in this study.

The depth of only the keyhole welds (solid symbols in Figs. 7A and 7B) are replotted in Fig. 10 vs. a "power factor" that incorporates the 0.625 slope. From this graph, the following relationship was derived for the penetration:

$$D = \left(\frac{1}{5.3}\right)\left(\frac{\alpha^{0.625}}{k\theta_M}\right)\left(\frac{P}{(Sf)^{0.625}}\right). \qquad (19)$$

Again, D is in mm, the material property units are summarized in Table 2, and the EB parameters are in units of mm, J and s. The constant factor C is 5.3, which is similar to the value of 3.3 determined by Giedt and Tallerico. The larger value found in this study results from the use of the focal spot diameter, f, instead of the surface fusion zone width, W.

Summary of EB Penetration Regimes

In summary, the results of this investigation indicate that the heating effect of an electron beam can behave in one of three different modes, depending on the energy density and power density of the electron beam.

The distributed-source welds have the lowest aspect ratios, and these can be modeled by a one-dimensional heat flow approximation. These welds are made at low energy densities (high travel speeds), where the heat diffuses primarily normal to the surface of the workpiece. The depth of penetration of these welds is given by Equation 16; it is directly proportional to the average energy density of the electron beam.

Welds that can be simulated by point-source heating have intermediate aspect ratios and are made at higher energy densities but at low enough power densities to prevent the formation of a vapor cavity. These welds have aspect ratios on the order of unity, which is characteristic of three-dimensional heat diffusion, and they can be modeled by the point-source theory. However, this theory indicates highly nonlinear behavior between weld pool shape and the typical welding parameter regime where point-source heating occurs. Because of this nonlinearity, the variation of depth with travel speed is related to the thermal properties of the workpiece. Therefore, separate equations are required to describe the penetration in Al and stainless steel alloys, as summarized by the different coefficients for the Al and stainless steel alloys in Equation 17.

Welds that can be simulated by line-source heating have the highest aspect ratios, and these welds are made at high energy densities and high power densities. These conditions create a vapor cavity and allow the heat to be deposited below the surface of the workpiece.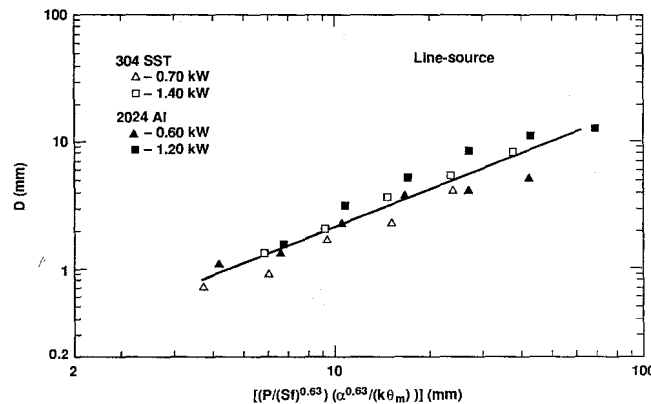 These line-source welds are characterized by deep penetrations, and the heat diffusion is primarily radially away from the line source in two dimensions. These welds occur when the energy density exceeds the critical value (~ 10 J/mm^2) and when the power density also exceeds a critical value of about 4 to 5 kW/mm^2. Under these conditions, the depth of penetration can be estimated by the relatively simple empirical relationship of Equation 19.

Conclusions

1) The influence of the EB welding parameters on the weld pool shape was determined for three power densities and for a wide range of energy densities. Figure 5 summarizes these findings by plotting the weld aspect ratio as a function of the average energy density for three different power density beams. These results show that both $\bar{E}_0$ and $\bar{P}_0$ can influence the weld pool shape.

2) The average energy density can be used to predict the transition from welds characteristic of a distributed heat source to those characteristic of a line heat source. For energy densities below a critical value ($\bar{E}_0 < \bar{E}^*_0$), the welds can be simulated by distributed-source heating ($\phi < 1$). In this regime, the penetration depends primarily on $\bar{E}_0$. For energy densities above the critical value ($\bar{E}_0 > \bar{E}^*_0$), the welds can be simulated by 1) line-source heating ($\phi > 1$) for high-power-density beams or 2) point-source heating ($\phi \sim 1$) for low-power-density beams. In this high-energy-density regime, the depth of penetration depends on both $\bar{E}_0$ and $\bar{P}_0$.

3) The critical energy density which separates the different heating modes, was shown to be a material-dependent parameter. This parameter was determined from the aspect ratio of the welds to be 6 J/mm^2 for 2024 Al and 10 J/mm^2 for 304 stainless steel.

4) Empirical relationships were developed between the penetration depth and the EB welding parameters for the distributed, point and line source heating modes. These relationships are presented in Equations 16, 17 and 19, respectively, and they can be used to predict the penetration depth of EB welds over a wide range on material processing parameters.

References

1. Rosenthal, D. 1946. The theory of moving sources of heat and its application to metal treatments. *Transactions ASME,* 43(11):849–866.
2. Christensen, N., Davies, V., and Gjermundsen, K. 1965. The distribution of temperatures in arc welding. *British Welding Journal,* 12(2):54–75.
3. Eagar, T. W., and Tsai, N. S. 1983. Temperature fields produced by traveling distributed heat sources. *Welding Journal,* 62(12): 346-s to 355-s.
4. Swift-Hook, D. T., and Gick, A. E. F. 1973. Penetration with lasers. *Welding Journal,* 52(11):492-s to 499-s.
5. Miayazaki, T., and Giedt, W. H. 1982. Heat transfer from an elliptical cylinder moving through an infinite plate applied to EB welding. *Int. J. Heat and Mass Transfer,* 25(6):807–814.
6. Giedt, W. H., and Tallerico, L. N. 1988. Prediction of electron beam depth of penetration. *Welding Journal,* 67(12):299-s to 305-s.
7. Elmer, J. W. 1988. The influence of cooling rate on the microstructure of stainless steel alloys. ScD Thesis, Dept. Materials Science and Engineering, *Massachusetts Institute Of Technology,* Cambridge, Mass.
8. Burgardt, P. 1989. Private communication and unpublished research.
9. Touloukian, Y. S., Powell, R. W., Ho, C. Y., and Klemens, P. G. 1972. *Thermophysical Properties Of Matter, Vols. 1 and 10,* Plenum Publishing Corp., New York, N. Y.

Fig. 10 — Depth of penetration for the line-source welds plotted vs. a dimensionless coordinate that incorporates the findings of Giedt and Tallerico (Ref. 6).

Appendix

Moving-Point-Source Depth of Penetration

The quasi-steady temperature distribution around a point source moving at velocity S along the surface of a semi-infinite solid is given by

$$\theta = T-T_0 = \left(\frac{P}{2\pi kR}\right)e\left(\frac{-S}{2\alpha}(R + X)\right), \qquad (A1)$$

where the heat source is moving in the positive X direction and $R = (X^2 + Y^2 + Z^2)^{1/2}$.

The temperature field represented by this relation can be visualized as a series of isothermal surfaces that are oval in shape, similar to one-half of an eggshell. The region enclosed by the melt isotherm, $\theta_M = T_M - T_0$, is the fusion zone, and this can be used to determine the maximum penetration, D, for a given set of welding parameters. This point occurs on the melt boundary, which is the furthest advancement of the liquid/solid interface from the point source.

The maximum distance of any isotherm below the surface will occur along the centerline of the weld at Y = 0. This location can be determined by setting the partial derivative of θ with respect to X equal to zero. The partial derivative of the point-source equation with respect to X is:

$$\frac{\partial \theta}{\partial X} = \frac{P}{2\pi k}\left[\left(\frac{1}{R}\right)e\left(\frac{-S}{2\alpha}(R + X)\right)\left(\frac{\partial R}{\partial X}+1\right)\right.$$
$$\left(\frac{-S}{2\alpha}\right) + e\left(\frac{-S}{2\alpha}(R + X)\right)\left(\frac{-1}{R^2}\right)\frac{\partial R}{\partial X}\right], \qquad (A2)$$

which can be solved for the maximum depth of penetration when it is evaluated on the melt isotherm. Using the subscript M to denote points that lie on the melt isotherm and rearranging terms gives the following expression:

$$\frac{\partial \theta_M}{\partial X} = \frac{-P}{2\pi k}\left(\frac{S}{2\alpha}\right)\left(\frac{1}{R_M}\right)\left(e\left(\frac{-S}{2\alpha}(R_M + X_M)\right)\right)$$
$$\left[1 + \frac{X_M}{R_M} + \frac{2\alpha X_M}{SR^2_M}\right], \qquad (A3)$$

which is equal to zero when the following algebraic equation is satisfied:

$$1 + \frac{X_M}{R_M} + \frac{2\alpha X_M}{SR^2_M} = 0. \qquad (A4)$$

This result can be arranged to give the following convenient relationship between the distance behind the heat source, X_{MB}, and the radial distance, R_{MB}, from the point source to the melt boundary. The second subscript, B, indicates those points on the melt isotherm that also lie on the melt boundary:

$$X_{MB} = \left(\frac{-SR^2_{MB}}{SR_{MB} + 2\alpha}\right). \qquad (A5)$$

Note that this equation cannot be solved directly for X_{MB}, since X_{MB} is a function of $R_{MB} = (X_{MB}^2 + Y_{MB}^2 + Z_{MB}^2)^{1/2}$. Also note that this expression does not directly involve the welding power or the material properties.

Equation A5 gives a relationship for the semicircular shaped liquid/solid boundary that would be observed in a metallographic cross-section of an ideal point-source weld. The maximum penetration is located on this boundary, and it is equal to Z_{MB} when $Y_{MB} = 0$. Therefore, one additional equation is required to solve for the maximum penetration.

Returning to the moving-point-source equation, X_{MB} is eliminated by substituting its value from Equation A5. By further setting $T = T_M$, the following expression for R_{MB} can be derived:

$$R_{MB} = \left(\frac{P}{2\pi k\theta_M}\right)e\left(\frac{-SR_{MB}}{SR_{MB} + 2\alpha}\right), \qquad (A6)$$

where R_{MB} must be determined using an iterative approach.

Once the radial distance to the melt boundary has been determined from Equation A6, X_{MB} can then be calculated from Equation A5. Finally, the maximum depth of penetration can be calculated from the Pythagoren identity:

$$D = (R^2_{MB} - X^2_{MB})^{1/2}. \qquad (A7)$$